JOURNAL OF MAGNETIC RESONANCE **125,** 92–101 (1997)
ARTICLE NO. MN961086

A Single-Scan Imaging Technique for Measurement of the Relative Concentrations of Fat and Water Protons and Their Transverse Relaxation Times

J. MA, F. W. WEHRLI,* H. K. SONG, AND S. N. HWANG

Department of Radiology, University of Pennsylvania Medical Center, 3400 Spruce Street, Philadelphia, Pennsylvania 19104

Received August 19, 1996; revised November 14, 1996

A two-component chemical-shift-imaging technique is described from which fat and water images can be obtained in a single scan and in the presence of an inhomogeneous field. In addition, the method provides transverse relaxation rates R_2 and R_2' separately for each of the spectral components. The method is a combination and extension of the GESFIDE [gradient echo sampling of FID and echo, J. Ma and F. W. Wehrli, *J. Magn. Reson. B* **111, 61 (1996)] and the multipoint Dixon techniques. It is based on sampling the descending and ascending portions of a Hahn spin echo with a train of gradient echoes which are spaced at one-half of the chemical-shift modulation period. Processing of the complex echo data, involving an automated phase unwrapping algorithm, affords relative amplitudes and transverse relaxation rates of the two spectral components. An additional benefit of the method is its superior signal-to-noise ratio resulting from echo summation. Applications targeted and illustrated involve MRI osteodensitometry of trabecular bone in the presence of varying fractions of hematopoietic and fatty bone marrow.**

INTRODUCTION

Image-based quantitation of the magnetic resonance (MR) transverse relaxation is of interest in blood oxygenation level dependent (BOLD) brain functional imaging (*1–4*), the determination of brain iron concentration (*5–7*), and the assessment of trabecular bone structure (*8–11*). The effective transverse relaxation rate R_2^* ($\equiv 1/T_2^*$), measured by a series of gradient echoes with varying echo times, can be expressed as a sum of two components: the irreversible contribution R_2 ($\equiv 1/T_2$) and the RF reversible contribution R_2' ($\equiv 1/T_2'$). Generally, R_2 is measured by a series of individual spin echoes or, more conveniently, by a train of Carr–Purcell–Meiboom–Gill (CPMG) echoes. R_2' can then be determined as the difference between R_2^* and R_2. Alternatively, R_2' can be obtained directly, e.g., by means of the asymmetric echo technique (*6, 11*), where the phase-reversal pulse in a $90°—\tau—180°—\tau$ spin-echo sequence is offset in time increments Δ. The resulting signal then evolves as $\exp(-2\Delta R_2')$, i.e., independently of R_2.

Since different physiologic processes may affect R_2, R_2', or both, the distinction between reversible and irreversible transverse relaxation is of considerable interest. An example is the BOLD effect which, because of the relative change in field perturbation by paramagnetic deoxyhemoglobin and the rate of diffusional motion, involves changes in R_2 for intravascular regions, R_2' for regions surrounding large vessels, and both R_2 and R_2' for tissues in the intercapillary space (*12, 13*). In contrast, the susceptibility-induced relaxation enhancement caused by trabecular bone is largely an R_2' effect since the thickness of the field-inducing trabeculae is much greater than the mean diffusional distance (*14*).

In addition to a separation of the reversible and irreversible transverse relaxation rates, situations exist, for example, in bone-marrow imaging, where knowledge of the volume fractions of fat and water is also important. R_2' of trabecular bone marrow is a function of the relative marrow composition as a result of the different magnetic susceptibilities of the two types of marrow (fatty vs hematopoietic). Separating water and fat is usually not possible with spin–warp imaging since it employs frequency encoding and thus does not distinguish among signals from the protons resonating at different frequencies. However, if data are acquired at more than one echo time, spectral information can be encoded into the time axis. In the case of a homogeneous B_0 field and negligible transverse relaxation, it has been demonstrated that sampling at two different time points at which the two spectral components have different relative phase orientation is sufficient for a complete water/fat separation (*15, 16*).

The situation becomes more complicated in the presence of magnetic field inhomogeneity. In this case, additional image acquisitions are required. In return, such approaches afford magnetic field maps and transverse relaxation rates as additional output parameters. Glover demonstrated that a complete characterization of a system with two spectral components is possible if echoes are sampled at more than

* To whom correspondence should be addressed.

1090-7807/97 $25.00

two time points (*17*). However, the so-called multipoint Dixon methods described have limitations. First, several acquisitions are required. Although these can be concatenated, the scan time scales in proportion to the number of time points for which data are taken. Second, the determination of both R_2^* and R_2' requires separate image acquisitions in both spin-echo and gradient-echo modes, leading to prohibitively long imaging time for any practical *in vivo* applications where such information is desired. Finally, the precision in determining the transverse relaxation rate is low since the time span over which data are sampled is short relative to typical tissue T_2^* or T_2' relaxation times (for example, one period of fat/water modulation is 4.6 ms at 1.5 T, compared to $T_2' \sim 20-50$ ms in trabecular bone marrow).

In this paper, a technique is presented in which parameter images of fat, water, R_2, and R_2' can be generated in a single scan. The technique is based on collecting the complex signals from two gradient-echo trains placed before and after a phase-reversal 180° RF pulse. The two echo trains have been shown to evolve with characteristic rate constants from which R_2 and R_2' can be computed (*18*). The post-processing strategy introduced provides enhanced precision in the determination of the transverse relaxation rates and improved SNR for the fat and water images. A preliminary account of this work was given in Ref. (*19*).

MATERIALS AND METHODS

Theoretical Basis

Suppose that following excitation, the signal is successively sampled at time intervals δ. The complex signal of the nth sample occurring at time $t = n\delta$ can then be expressed as (*17*)

$$S_n = [A_1(n\delta)\rho_1 + (-1)^n A_2(n\delta)\rho_2]e^{i(n\phi+\phi_0)}. \quad [1]$$

In Eq. [1], $\phi = \gamma\Delta B(\mathbf{r})\delta$ is the phase shift induced between two successive echoes by magnetic field inhomogeneity ΔB at location $\mathbf{r}$, and ϕ_0 is a frequency-independent phase offset. It is further assumed that echoes are sampled only at time points when the fat and water signals are either parallel or anti-parallel, and the interecho time δ is set to one-half the water/fat modulation period. Quantities ρ_1 and ρ_2 represent the concentrations of the protons in water and the CH_2 protons in fat, respectively. If the pulse sequence is run under conditions of partial saturation, the resulting proton concentrations will be T_1-weighted. Quantities A_1 and A_2 are the amplitude loss factors for water and fat, which depend on the time of the sampling ($n\delta$) and the governing transverse relaxation rates. In the currently proposed technique, the amplitude loss factors are $A_{1,2}(n\delta) = e^{-n\delta R_{2_{1,2}}^*}$ for sampling the FID, and $A_{1,2}(n\delta) = e^{-n\delta R_{2_{1,2}}^-}$ for sampling the signal after the 180° refocusing pulse, where $R_2^- = R_2 - R_2'$ (see Pulse Sequence and Implementation below).

As mentioned earlier, when fat and water transverse relaxation and the inhomogeneity of the external field are negligible ($A_1 = A_2 = 1$ and $\phi = 0$), Eq. [1] can be solved by taking measurements at two time points (*15, 16*). If these conditions are not satisfied, measurements at additional time points are needed (*17, 20, 21*).

In the case where the transverse relaxation rates for the two spectral components are assumed to be equal ($A_1 = A_2 = A \neq 1$), sampling at three different time points ($n = 0, 1, 2$) yields, according to Eq. [1],

$$S_0 = (\rho_1 + \rho_2)e^{i\phi_0} \quad [2a]$$

$$S_1 = (\rho_1 - \rho_2)Ae^{i(\phi+\phi_0)} \quad [2b]$$

$$S_2 = (\rho_1 + \rho_2)A^2e^{i(2\phi+\phi_0)}. \quad [2c]$$

Equations [2a]–[2c] can be solved analytically and the exact solutions are given as

$$A = \sqrt{\frac{|S_2|}{|S_0|}} \quad [3]$$

$$2\phi = \arg\left(\frac{S_2}{S_0}\right) \quad [4]$$

$$\rho_1 = 0.5|S_0|\left\{1 + \zeta\frac{|S_1|}{\sqrt{|S_0||S_2|}}\right\} \quad [5]$$

$$\rho_2 = 0.5|S_0|\left\{1 - \zeta\frac{|S_1|}{\sqrt{|S_0||S_2|}}\right\}, \quad [6]$$

where ζ is a switch function that can assume a value of either 1 or -1, depending on whether in a given voxel the water fraction ρ_1 is greater or less than the fat fraction ρ_2. The value of ζ is thus a function of the phase value ϕ and can be conveniently chosen as

$$\zeta = \cos\left[\arg\left(\frac{S_1}{S_0}\right) - \phi\right]. \quad [7]$$

As shown in Eq. [3], the amplitude loss factor, and therefore the transverse relaxation rate, is determined by the ratio of the two in-phase amplitude images. Since the difference between the corresponding echo times is small (4.6 ms at 1.5 T, for example), the relative uncertainty in the transverse relaxation times (typically 20–50 ms) is large, especially at low SNR. From an SNR point of view, Eqs. [5] and [6] are not optimal since they involve nonlinear operations of images collected at three different echo times. It has been shown that when $A \approx 1$, the following approximate solutions, yielding better SNR, can be used:

$$\rho_1 = 0.5\{0.5(|S_0| + |S_2|) + \zeta|S_1|\} \quad [8]$$

$$\rho_2 = 0.5\{0.5(|S_0| + |S_2|) - \zeta|S_1|\}. \quad [9]$$

In this case, SNR corresponds to the equivalent of 2.67 signal averages (relative to a theoretical optimum of 3) (*17*).

The three-point analysis is valid only for equal transverse relaxation rates for the two spectral components. If $A_1 \neq A_2$, a measurement at a fourth time point ($n = 3$) is necessary for deriving all parameters from Eq. [1]. However, because of its nonlinearity, the equation cannot be solved analytically. By expanding Eq. [1] using the approximation $A = e^{-\epsilon} \approx 1 - \epsilon$, Glover derived the following set of solutions for ρ_1, ρ_2, A_1, and A_2:

$$\rho_1 = S_0''/2 + (3S_1'' - S_3'')/4 \quad [10a]$$

$$\rho_2 = S_0''/2 - (3S_1'' - S_3'')/4 \quad [10b]$$

$$A_1 = [S_1'' + (S_2'' + S_0'')/2]/2\rho_1 \quad [10c]$$

$$A_2 = (\rho_1 A_1 - S_1'')/\rho_2, \quad [10d]$$

where $S_n'' \equiv S_n e^{-i(n\phi+\phi_0)}$. Besides being valid only on condition of small amplitude loss, Eqs. [10a]–[10d] afford very poor SNR performance (*17*). The multiecho oversampling technique discussed below offers an alternative processing strategy. On the assumption that the transverse relaxation rates are equal for the two spectral components ($A_1 = A_2$), ρ_1 and ρ_2 images can be generated from groups of three consecutive echoes ($S_0/S_1/S_2$, $S_2/S_3/S_4$, $S_4/S_5/S_6$, etc.). Since the resulting ρ_1 and ρ_2 values are weighted by their respective echo times, the transverse relaxation rates for fat and water can be determined directly without solving the nonlinear and coupled equation (Eq. [1]). The errors in ρ_1 and ρ_2 at different echo times caused by assuming equal transverse relaxation rates for the two components can, in principle, be corrected by an iterative process in which new sets of ρ_1 and ρ_2 are calculated with the previously determined A_1 and A_2. For tissue parameters typical of fat and water, however, it will be seen that the errors in ρ_1 and ρ_2 are negligibly small and do not cause any significant errors in the derived transverse relaxation rates.

Imaging

Pulse sequence and implementation. The pulse sequence employed does not differ from the original GESFIDE pulse sequence (*18*) except that the interecho time between successive gradient echoes was set to one-half of the fat–water chemical-shift modulation period. The principle is to alternately sample in-phase and opposed-phase echoes which, in addition to the chemical-shift modulation, evolve with rate constants $R_2^* = R_2 + R_2'$ during the first τ period, and $R_2^- = R_2 - R_2'$ during the second τ period. In a typical embodiment, eight echoes each were generated before and after the phase reversal RF pulse. Under the assumption of equal transverse relaxation rates for the two spectral components, R_2 and R_2' were derived from the average of the two results from regressions to the modulation-free in-phase and opposed-phase echo amplitudes. Chemical-shift-selective images for water and fat protons (ρ_1 and ρ_2) were obtained separately from groups of three consecutive echoes ($S_0/S_1/S_2$, $S_2/S_3/S_4$, etc.) via either Eqs. [8] and [9] or Eqs. [5] and [6] as specified and combined subsequently to improve SNR, as detailed in the following section.

The pulse sequence (Fig. 1) was implemented on a 1.5 T General Electric Signa whole-body scanner operating in 5.2.ufi configuration. The system was equipped with a prototype whole-body gradient system, providing 152 μs rise time from zero to the maximum gradient strength of 2.2 G/cm on all three axes. In order to minimize the sensitivity of the signal to global background field gradients, only echoes of positive polarity were collected. Operation at $\pm$64 kHz receiver bandwidth and 128 readout points permitted a first echo time of 4.6 ms at which fat and water are in phase, and successive echoes spaced 2.3 ms apart. Coronal abdominal images encompassing the proximal femur and sagittal images of the spine were collected from different volunteers with their consent and under a protocol approved by the Institutional Review Board at the authors' institution.

Signal Processing

Phase unwrapping. Processing of the acquired images was achieved in several steps: first, the complex images corresponding to the first two in-phase echoes in the gradient-echo train preceding the phase-reversal RF pulse were used to generate a phase map according to Eq. [4]. Since the resulting phase values are restricted between $-\pi$ and π, phase wrapping occurs in regions of high field inhomogeneity or low SNR. Therefore, a phase unwrapping algorithm was implemented to obtain an unaliased phase map from which the switch function ζ can be determined via Eq. [7].

Various methods have been devised for the seemingly simple task of restoring a wrapped phase map (*22*). The strategy adopted in the current work follows the approaches of the simple nonparametric region growing (*21*) and polynomial extrapolation (*23*), and is based on the observation that phase unwrapping based on region growing is problematic only for regions of low SNR or where artifacts are present. To proceed, spatial derivatives with respect to x and y coordinates of the phase map were first calculated, and a preselected threshold value for the derivatives was chosen to separate the phase map into high- and low-noise regions, based on the interpixel phase variations (modulo 2π). To facilitate the unwrapping process, each low-noise pixel was assigned two values l_x and l_y, representing the total number of the connected low-noise pixels along x and y, respec-

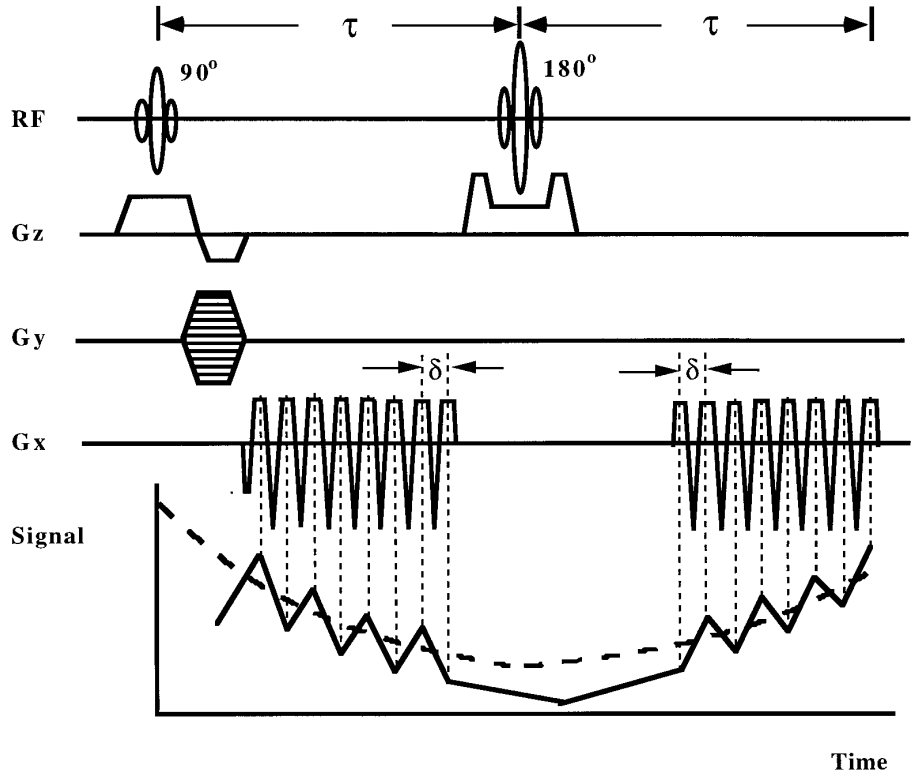

FIG. 1. GESFIDE pulse sequence for simultaneous two-component chemical-shift imaging and measurement of relaxation rates R_2 and R_2'. In addition to the fat/water modulation, the signal evolves with rate constants $R_2^* = R_2 + R_2'$ during the first τ period and $R_2^- = R_2 - R_2'$ during the second τ period. In the preferred embodiment, echoes of equal polarity are sampled with an interecho spacing δ of one-half of the chemical-shift modulation period (2.3 ms at 1.5 T for fat and water).

tively. With this preprocessing, a seed point was chosen as the center pixel having the largest l_x or l_y values. Phase unwrapping of the low-noise region was initiated from the seed point and then propagated, using l_x and l_y as loop indices, by comparing the phase difference of each pair of neighboring pixels and removing multiples of 2π when necessary. For the high-noise pixels, phase unwrapping was accomplished through comparison of the actually measured values with those obtained by linear interpolation or extrapolation, based on the unwrapped low-noise pixel values (*23*). Multiples of 2π were added or subtracted whenever necessary from the actually measured phase values, depending on the difference between the predicted and the measured values.

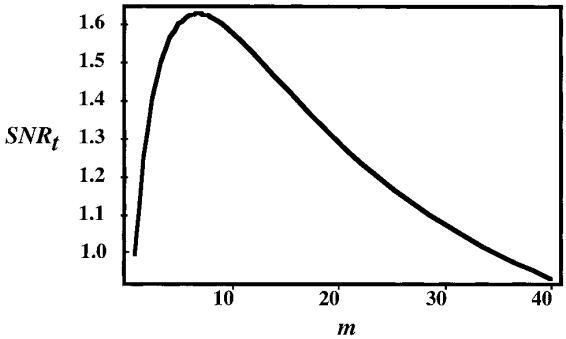

FIG. 2. Effective SNR resulting from echo summation vs the total number of coadded echoes m. SNR plotted is relative to that from the first echo, and signal from subsequent echoes is assumed to decrease with a time constant $1/R_2^* = 50$ ms.

Calculation of transverse relaxation rates and component images. Two situations, where fat and water have either the same or different transverse relaxation rates, were considered. In the first situation, Eq. [1] shows that R_2^* and R_2^- (thus, R_2 and R_2') can be determined by linear regression of the logarithms of the amplitudes of the in-phase echo signals preceding and following the 180° refocusing pulse, as in the original GESFIDE implementation. Likewise, the out-of-phase signals can be processed to yield a second data set, though SNR is compromised in regions where ρ_1 and ρ_2 are comparable in magnitude. In contrast to the original three-point Dixon method (Eq. [3]), the current method offers superior precision, which results from the increased number of sampling points and the increased time span for signal evolution (*24*).

To obtain separate fat and water images, the data from the echo train preceding the 180° pulse were arranged in

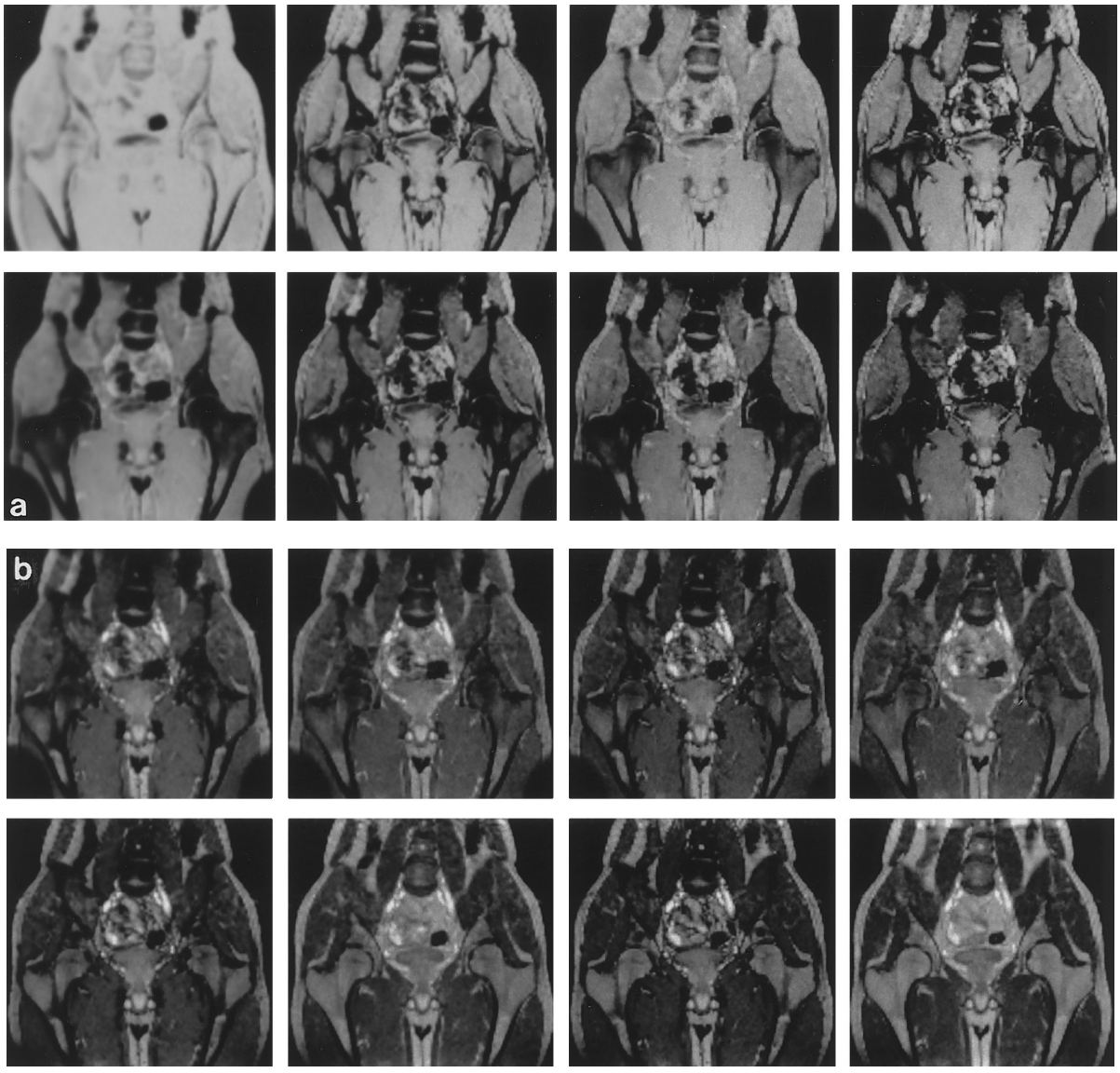

FIG. 3. GESFIDE images acquired from a 27-year-old male volunteer (interecho spacing = 2.3 ms, τ = 30 ms, TR = 1.2 s, FOV = 40 cm, matrix size = 128 × 256, slice thickness = 5 mm with 2 mm interslice spacing; scan time = 10 min): (a) echoes preceding, and (b) echoes following the phase-reversal RF pulse. The echoes are spaced at one-half of the fat–water chemical-shift modulation period. An alternation in signal amplitude between successive echoes is noticeable for tissues with comparable fractions of fat and water, such as the vertebrae and portions of the femur. Also visible is the partial return of the signal in the bone marrow, which indicates the reversible nature of signal decay for these magnetically inhomogeneous tissues (b).

groups of three each: $S_0/S_1/S_2$, $S_2/S_3/S_4$, $S_4/S_5/S_6$. Three sets of fat and water images were then generated according to Eqs. [8] and [9], and coadded to yield an SNR-enhanced set of water and fat images (ρ_{1t} and ρ_{2t}). On the simplifying assumption that noise is uncorrelated, the echo summation described increases SNR when the conditions specified below are satisfied. Since the signals from different groups of echoes are weighted by different decay times, the resulting SNR from m echo groups becomes

$$\text{SNR} = \frac{s_1(1 + A^3 + A^6 + \cdots + A^{3(m-1)})}{n_1\sqrt{m}} = \frac{s_1}{n_1} \cdot \frac{1 - A^{3m}}{(1 - A^3)\sqrt{m}}, \quad [11]$$

where s_1/n_1 is the SNR for the first set of echoes. According to Eq. [11], SNR depends on the amplitude loss factor $A = \exp(-R_2^* \delta)$ and m, the total number of echo groups. In Fig.

2, the dependence of the relative SNR on m is plotted for $1/R_2^* = 50$ ms. It is evident that echo coaddition improves SNR significantly, reaching an optimum which, under the current assumptions, occurs for $m \sim 9$. Thereafter SNR decreases since losses from signal decay prevail over the SNR gain from coaddition.

If the transverse relaxation rates differ for the two spectral components (i.e., $A_1 \neq A_2$), R_2 and R_2' can be obtained from sets of ρ_1 and ρ_2 determined from Eqs. [5] and [6]. Although the errors in the resulting transverse relaxation rates can be corrected with further iterations, such correction is not necessary for typical fat and water relaxation parameters. Suppose equal fat and water proton concentration and $T_{2,\text{water}} = 35$ ms and $T_{2,\text{fat}} = 80$ ms, the errors in ρ_1 and ρ_2 as determined from Eqs. [5] and [6] were found to be on the order of 2%. The T_2 relaxation times, which are determined by the ratio of the apparent ρ_1 and ρ_2 values computed from different groups of echoes (e.g., $S_0/S_1/S_2$, $S_2/S_3/S_4$, $S_4/S_5/S_6$), were found to be 34.8 and 79.1 ms for water and fat respectively, i.e., within about 1% of the actual values.

All image processing was carried out on a SPARC 10 workstation (Sun Microsystems, Inc., Mountain View, California) using the IDL software (Research Systems, Inc., Boulder, Colorado).

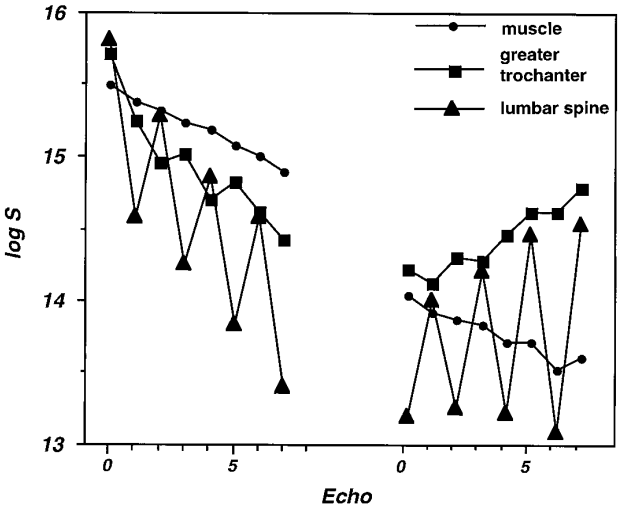

FIG. 4. Semi-logarithmic plot of gradient-echo ROI signal amplitudes for three different tissues versus echo number as derived from the images of Fig. 3. Sixteen echoes were collected, eight before and eight after the phase-reversal RF pulse. The predominantly fatty marrow in the greater trochanter shows only slight modulation, whereas the mixed marrow in the vertebrae causes strong amplitude modulation. Note smooth continuous decay for gluteal muscle.

RESULTS AND DISCUSSION

Figure 3 shows a series of coronal GESFIDE amplitude images from one of five slices acquired in a single scan using the pulse sequence of Fig. 1. The images correspond to 16 alternating in-phase and anti-phase echoes, 8 on each side of the 180° refocusing pulse, and were reconstructed from the raw data after zero filling to a 256 × 256 matrix size and Fermi filtering. One notices the intensity void in the opposed-phase images for pixels abutting fat and water, an effect caused by signal cancellation due to comparable fractions of fat and water in the boundary voxels. Also noticeable, as demonstrated in the original GESFIDE experiment (*18*), is the RF-reversible nature of the signal amplitude for tissues with large intrinsic R_2', such as trabecular bone marrow in the femur and the vertebrae. In contrast, tissues without intrinsic inhomogeneity, such as muscle, exhibit a continuous decay. Figure 4 shows region-of-interest plots of the signal amplitudes of the 16 successive echoes versus echo time for three different anatomic locations. Whereas the amplitude essentially varies monotonically for the greater trochanter and the gluteal muscle, it oscillates in the lumbar vertebra L5 owing to the presence of the comparable amounts of fat and water in vertebral marrow.

Figure 5a displays the original phase map computed from Eq. [4]. Phase aliasing is apparent in several locations across the FOV where field deviations are large or SNR is low. Figure 5b shows the corrected phase image, obtained by applying the unwrapping algorithm presented under Materials and Methods. Assuming equal transverse relaxation rates for water and fat, the water and fat fractions can be obtained from the three-point analysis described previously (Eqs. [5] and [6]) and the transverse relaxation rates can be determined by regression of the logarithms of the in-phase or opposed-phase image amplitudes. Figures 5c and 5d display the water and fat images which demonstrate that consistent water/fat separation is achieved over the entire field of view despite the presence of large magnetic field inhomogeneities. Figures 5e and 5f represent co-added water and fat images from three subsets of component images pertaining to the echo train before the 180° pulse. In comparison to the component images derived from a first set of source images (Figs. 5c and 5d), the coadded images exhibit superior SNR (Figs. 5e and 5f). In the water image, for example, SNR (defined as average over the standard deviation for the same ROI) in gluteal muscle was approximately 40% higher in the co-added image than in the component image (35 vs 25 in one typical ROI, for example). Since the three sets of component images are derived from groups of source images, one of which is shared among groups, their noise is not completely uncorrelated. Consequently, the SNR gain from the echo summation is expected to be lower than predicted by Eq. [11]. It is further noted from Eq. [11] that there is less gain from image summation for fast relaxing species, and therefore the summation images show contrast enhancement.

In order to assess the accuracy of the fat and water separation, localized spectroscopy using the standard STEAM sequence was performed in several representative locations of

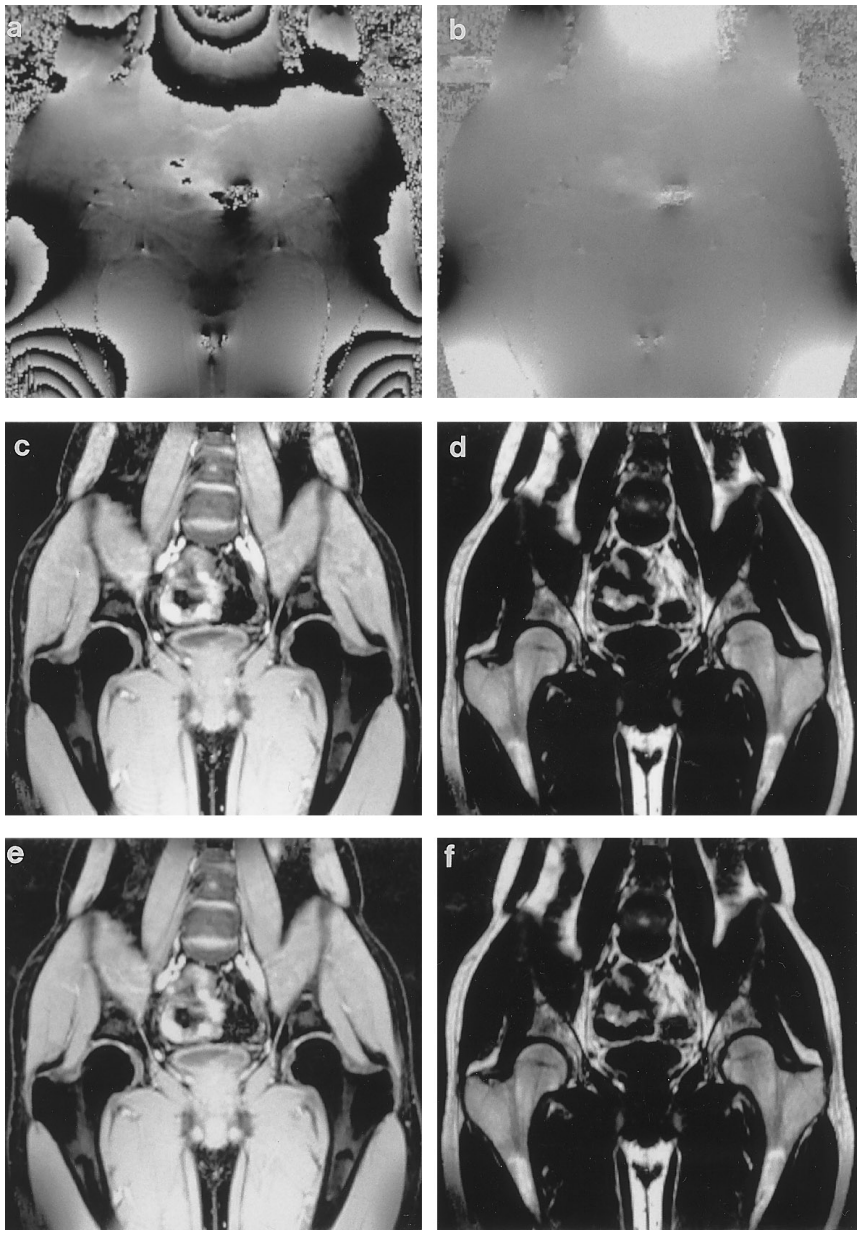

FIG. 5. Processing steps in the analysis of the source images. (a) Phase map computed from echoes S_0 and S_2, showing aliasing in areas of large field gradients. (b) Corrected phase image obtained by phase unwrapping using the algorithm described under Materials and Methods. (c–f) Component images: (c, e) water images and (d, f) fat images. Images (c, d) were derived from the first three echoes (S_0, S_1, S_2), while images (e, f) represent the corresponding co-added images which exhibit enhanced contrast and SNR. Note that the component images show consistent water/fat separation despite significant field inhomogeneities.

the same volunteer. An 11.2 × 11.2 × 6 mm ROI was selected at each location. In order to ensure equal saturation for the imaging and spectroscopy experiment, TR = 1200 ms was chosen, whereas for the echo time in the spectroscopic measurements the minimum TE of 32 ms was used. The resulting fat/water proton concentration ratios, along with those from the first set of the component images (Fig. 5c and Fig. 5d) are shown in Fig. 6. Very good agreement is generally found for the two different methods in anatomic regions of varying fat/water concentrations, except for the femoral head. The discrepancy is not fully understood presently and may be due to a mismatch in the ROI location between the two different experiments.

The decay rates R_2^* and R_2^- were determined from the amplitudes of the echoes occurring before and after the 180° pulse, respectively, as described under Materials and Methods. The first in-phase echo amplitude value was excluded in the regression because it was found to have abnormally

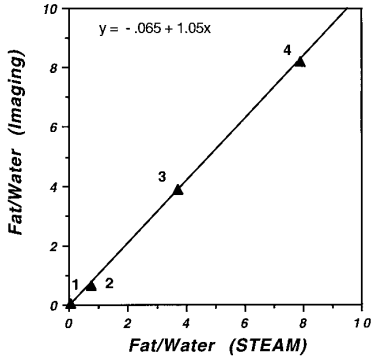

FIG. 6. A comparison of the fat/water proton density ratio, obtained by the present imaging technique and by STEAM localized spectroscopy, showing excellent agreement: 1, muscle; 2, lumbar vertebra; 3, femoral shaft; 4, subcutaneous fat. The data point representing the femoral head was excluded.

high intensity for subcutaneous fat. This phenomenon is attributed to modulation from the protons α to the carboxyl group and allylic protons which have short T_2. Since their signal decays rapidly and irreversibly, it only contributes significantly to the first echo [see, for example, Ref. (*25*)]. The resulting R_2, R_2', and R_2^* images are presented in Figs. 7a, 7b, and 7c. The R_2^* image exhibits enhanced intensity primarily in regions rich in trabecular bone, consistent with the susceptibility-induced line broadening in this structure. This effect is found to be more pronounced in the R_2' images.

Fat and water have different magnetic susceptibilities; therefore, the susceptibility-induced relaxation rate (R_2') in the same trabecular bone network would, in principle, depend on the relative concentration of the two constituents and, further, their microscopic distributions. Several scenarios are possible. (1) The two constituents are homogeneously mixed in the marrow spaces: In this case, rates R_{2w}' and R_{2f}' are the same (albeit being functions of the relative volume fractions of the two constituents). (2) The relative concentrations are spatially variant. For example, there might be more hematocytes near the trabecular surface, in which case the water protons would be exposed to higher gradient fields than their fat counterparts, and R_{2w}' would be greater than R_{2f}'. (3) The two marrow types could be sequestered, in which case R_2' for the two constituents would again differ. The trans-

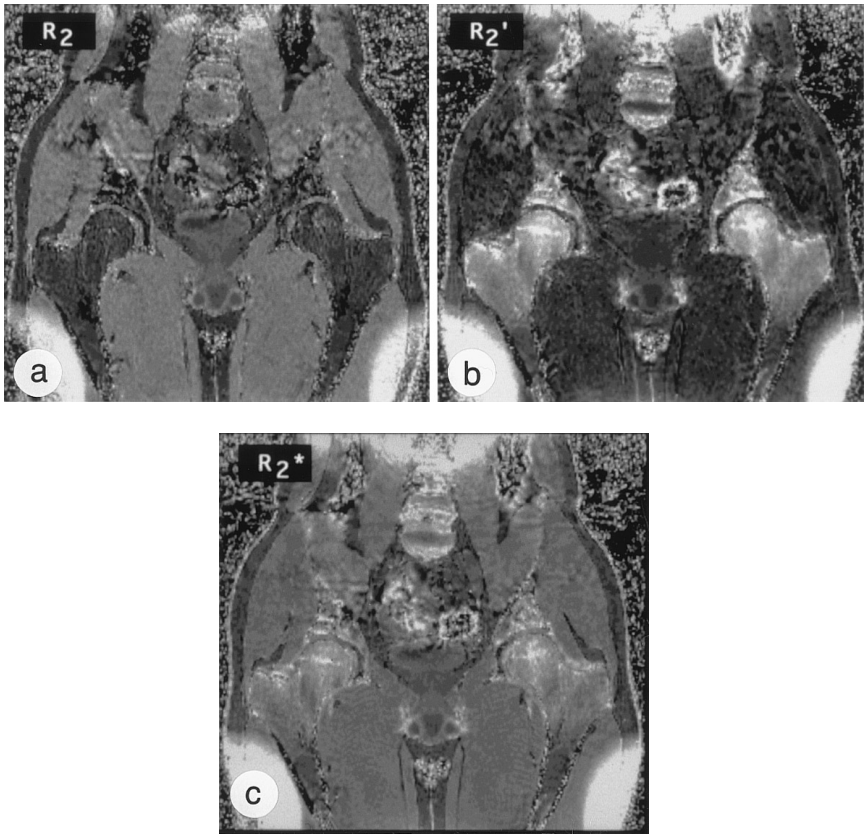

FIG. 7. Relaxation rate images derived from the source images of Fig. 3: (a) R_2, (b) R_2', (c) R_2^*. Images were computed as averages of the rates obtained by regression of the in-phase and opposed-phase images assuming equal transverse relaxation rates for the two spectral components. Increased R_2' (and to a lesser extent R_2^*) is noted in bone marrow regions where trabeculation is significant (e.g., femoral head, neck, greater trochanter, but not in the femoral shaft). The spurious enhancement at the top and in the lower left and right corners is caused by poor shimming in these regions, as is evident in the phase maps (Figs. 5a–5b).

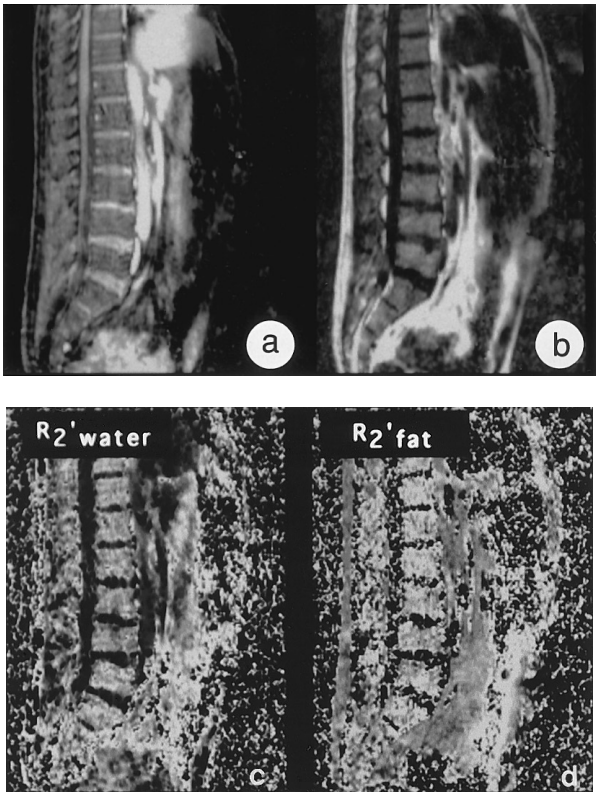

FIG. 8. Relaxation rates for individual spectral components (fat and water) calculated from sets of relaxation-weighted water and fat images. Each set was derived from a different group of echoes ($S_0/S_1/S_2$, $S_2/S_3/S_4$, $S_4/S_5/S_6$) collected with the pulse sequence of Fig. 1. To minimize the effect of abdominal motion, a 60 mm thick sagittal spatial presaturation pulse was placed before excitation. (a) Water image, (b) Fat image, (c) R'_{2w}, and (d) R'_{2f}. R'_2 is comparable for water and fat; however, precision of the component relaxation maps is low.

verse relaxation rate would then be a function of the volume distribution and shape of the compartments.

Figures 8a and 8b show component water and fat images determined from the first three gradient echoes according to Eqs. [5] and [6]. Figures 8c and 8d show maps of R'_{2w} and R'_{2f} obtained as described previously. Relaxation rate images demonstrate high noise wherever the corresponding proton density is low. In regions where fat and water coexist at comparable concentrations (e.g., vertebrae), finite values were obtained for both R'_{2w} and R'_{2f}. Preliminary data collected from two young healthy male volunteers (aged 26 and 28) showed R'_{2w} and R'_{2f} to be similar at given locations in most vertebrae (T11–L5). This observation implies a relatively homogeneous distribution of the two chemical constituents within the imaging voxels.

CONCLUSIONS

The method presented in this work is more efficient than previously reported two-component chemical-shift-imaging techniques that are based on collection of three or four sampling points (*17, 20, 21*). Oversampling, along with the described data processing strategy, increases SNR for the fat/water images and the precision in the derived transverse relaxation rates. The improvement in efficiency is readily understood when considering that data are collected continuously as long as signal is available, and the resulting data are processed constructively. Since at a given pixel size, the ultimate SNR is determined by the total sampling time, the loss in SNR associated with the use of higher bandwidth is recovered by echo summation. At the same time, increased receiver bandwidth minimizes chemical-shift misregistration, lowers the sensitivity to field inhomogeneity, and reduces point spread function blurring.

Another salient feature of the technique is the tissue contrast in the co-added images. While the images derived from 3-point processing are weighted by a simple factor $e^{(-TE/T2)}$, the co-added images exhibit enhanced relaxation-weighted contrast, as is evident from Eq. [11]. For example, R_2^* in trabecular yellow marrow (fat) is much greater than R_2^* in the femoral shaft. As a result, signal enhancement from echo summation will be greater in the latter region (cf. Fig. 5f). Such variation in relaxation parameters improves tissue visualization. At the same time, it precludes simultaneous optimization over the entire image using simple echo summation. The problem can be addressed by weighted echo summation. An optimal final image can thus be obtained by summing all available echoes, with increasing weighting for pixels corresponding to shorter transverse relaxation times or lower SNR.

A model-inherent source of error in the quantitation of the fat and water by all the Dixon techniques is incorrect setting of the interecho spacing. Failure to set the latter at exactly half the fat/water modulation period causes an increase in the out-of-phase signal amplitude, resulting in an underestimation of the lesser of the two components. A different source of systematic error is the presence of multiple resonance lines in the triacyl glyceride spectrum. The olefinic protons in fat resonate at 5.4 ppm (relative to tetramethylsilane), and their phase is thus very close to the water protons at 4.8 ppm, leading to a small overestimation of the water proton concentration. Another source of error is the different transverse relaxation rates, for example, between the major fatty acid CH_2 protons at 1.3 ppm and those α to the carboxyl group and α to the carbon–carbon double bond (both resonating in the range of 2–2.5 ppm). Since the latter have less segmental motion (i.e., longer correlation times), their T_2 relaxation times are shorter, which causes a rapid initial decay of the signal, and thus deviation from monoexponential behavior (cf. Fig. 4). In principle, such a systematic error can be corrected by making use of prior knowledge related to the triglyceride spectrum.

In conclusion, the pulse sequence presented permits effective separation of fat and water, and determination of their

reversible and irreversible transverse relaxation rates, in a single scan. Multiecho sampling along with the described processing strategy increases the precision in the transverse relaxation rates and SNR of the fat and water images relative to other multipoint Dixon techniques. In addition to greatly reduced scan time, the transverse relaxation rate measurement has the further advantage of being immune to RF pulse imperfections, as demonstrated previously (*18*). The technique should thus be particularly useful for *in vivo* evaluation of disease processes entailing alterations in both R_2 and R_2', such as bone and marrow disorders.

ACKNOWLEDGMENTS

The authors thank Dr. Jeffrey Hopkins for helpful discussions and Arijitt Borthakur and Linda Kalb for help in carrying out the experiments. This work was financially supported by National Institutes of Health through Grants RO1 AR 40671 and RO1 AR 41443.

REFERENCES

1. S. Ogawa, D. W. Tank, R. Menon, J. M. Ellerman, K. Seong-Gi, H. Merkle, and K. Ugurbil, *Proc. Natl. Acad. Sci.* **89,** 5951 (1992).
2. P. A. Bandettini, E. C. Wong, R. S. Hinks, R. S. Tifofsky, and J. S. Hyde, *Magn. Reson. Med.* **25,** 390 (1992).
3. K. K. Kwong, J. W. Belliveau, D. A. Chesler, I. Goldberg, R. Weisskoff, B. Poncelet, D. Kennedy, B. Hoppel, M. Cohen, R. Turner, H. Cheng, T. Brady, and B. Rosen, *Proc. Natl. Acad. Sci.* **89,** 5675 (1992).
4. R. S. Menon, S. Ogawa, D. W. Tank, and K. Ugurbil, *Magn. Reson. Med.* **30,** 380 (1993).
5. B. Drayer, P. Burger, R. Darwin, S. Riederer, R. Herfkens, and G. A. Johnson, *Am. J. Roentgenol.* **147,** 103 (1986).
6. G. Wismer, R. Buxton, B. Rosen, C. Fisel, R. Oot, T. Brady, and K. Davis, *J. Comput. Assist. Tomogr.* **12,** 259 (1988).
7. R. J. Ordidge, J. Gorell, J. Deniau, R. A. Knight, and J. A. Helpern, *Magn. Reson. Med.* **32,** 335 (1994).
8. F. W. Wehrli, J. C. Ford, M. Attie, H. Y. Kressel, and F. S. Kaplan, *Radiology* **179,** 615 (1991).
9. J. C. Ford and F. W. Wehrli, *Magn. Reson. Med.* **17,** 543 (1991).
10. S. Majumdar, D. Thomasson, A. Shimakawa, and H. K. Genant, *Magn. Reson. Med.* **22,** 111 (1991).
11. S. Majumdar and H. K. Genant, *J. Magn. Reson. Imaging* **2,** 209 (1992).
12. R. M. Weisskoff, C. S. Zuo, J. L. Boxerman, and B. R. Rosen, *Magn. Reson. Med.* **31,** 601 (1994).
13. R. P. Kennan, J. Zhong, and C. Gore J, *Magn. Reson. Med.* **31,** 9 (1994).
14. D. A. Yablonskiy and E. M. Haacke, *Magn. Reson. Med.* **32,** 749 (1994).
15. R. E. Sepponen, J. T. Sipponen, and J. I. Tanttu, *J. Comput. Assist. Tomogr.* **8,** 585 (1984).
16. W. T. Dixon, *Radiology* **153,** 189 (1984).
17. G. H. Glover, *J. Magn. Reson. Imaging* **1,** 521 (1991).
18. J. Ma and F. W. Wehrli, *J. Magn. Reson. B* **111,** 61 (1996).
19. J. Ma, F. W. Wehrli, S. Hwang, and H. K. Song, Abstracts of the International Society of Magnetic Resonance in Medicine, New York, p. 1571, 1996.
20. H. N. Yeung and D. W. Kormos, *Radiology* **159,** 783 (1986).
21. J. Szumowski, W. R. Coshow, F. Li, B. Coombs, and S. F. Quinn, *Magn. Reson. Med.* **34,** 120 (1995).
22. T. R. Judge and P. J. Bryanston-Cross, *Opt. Lasers Eng.* **21,** 199 (1994).
23. G. H. Glover and E. Schneider, *Magn. Reson. Med.* **18,** 371 (1991).
24. P. R. Bevington and D. K. Robinson, ''Data Reduction and Error Analysis for the Physical Sciences,'' 2nd ed., McGraw–Hill, New York, 1992.
25. F. Schick, B. Eismann, W. I. Jung, H. Bongers, M. Bunse, and O. Lutz, *Magn. Reson. Med.* **29,** 158 (1993).